# 3-D Metamaterial Based Terahertz Planoconcave Lenses for Linearly and Circularly Polarized Waves

**Muthusamy Marishwari[1], Venkatachalam Subramanian[2],**
**Zhengbiao Ouyang[3], and Natesan Yogesh[4, *]**

**Abstract**—A three-dimensional negative index (NI) metamaterial (MTM) is realized at terahertz (THz) frequencies. The structure is composed of orthogonally oriented cross-bars with arrows on each corner embedded in a dielectric cube. The proposed 3-D MTM is symmetric along all the principal axes and shows a polarization-insensitive, wide-incident-angle negative refractive index regime centered at 0.862 THz with an operational bandwidth of 0.234 THz (27.15%). Using staircase approximation, the proposed 3-D NI MTM has been designed into a THz parabolic planoconcave lens (PCL). A PCL made of a NI medium is a counterpart of a positive index planoconvex lens and focuses on the near-field region. The designed PCL shows 3-D focusing functionality for linearly and circularly polarized THz waves at 0.85 THz. The designed PCL has a short focal length and high numerical aperture (NA) with sub-wavelength focusing spot sizes. The computed FWHMs along transversal directions are $0.46\lambda(x) \times 0.49\lambda(y)$ for transverse electric (TE) polarized wave, $0.46\lambda(x) \times 0.49\lambda(y)$ for left-circularly polarized (LCP) wave, and $0.50\lambda(x) \times 0.42\lambda(y)$ for right-circularly polarized (RCP) wave, respectively. The corresponding back focal lengths of the realized PCLs are $1.07\lambda$, $1.03\lambda$, and $0.98\lambda$, and the focal depths are $0.40\lambda$, $0.48\lambda$, and $0.41\lambda$ for linear, LCP, and RCP waves, respectively. A short review of recent progress in manufacturing techniques for the fabrication of the proposed 3-D MTM is further highlighted. Since the proposed 3-D MTM PCL configurations show the far-field focusing of linearly/circularly polarized waves, imaging with high optical power requirements can be met for THz waveband applications.

## 1. INTRODUCTION

Electromagnetic (e-m) metamaterials (MTMs) are artificial, effective-homogenous structures with unusual properties such as negative refractive index and giant optical activity. Metamaterials provide alternative ways to manipulate light with control over amplitude, phase, and polarization. Owing to MTM's dimensions, ultra-thin, lightweight, and compact optical elements with sub-wavelength features can be realized in comparison with conventional optical systems. MTMs can fulfill the need to realize terahertz (THz) optical components. The THz band [1, 2] lies between the infrared and microwave regimes, and its frequency range is spanned from 0.1 THz to 10 THz. THz technology has experienced significant growth owing to its potential applications, including medical diagnoses, imaging, security, communication, and non-destructive sensing [3–6]. However, realizing THz components is mostly restricted with nonlinear materials, and the availability of natural media with THz response is limited.

Recent studies in THz bulk MTM structures [7–9] along with the developments in generating and detecting terahertz waves show that these constraints can be reduced for realizing THz devices.

Especially, an MTM with a negative index of refraction [10, 11], where the relative dielectric permittivity ($\varepsilon_r$) [12] and relative magnetic permeability ($\mu_r$) [13] are simultaneously negative and can potentially shape THz beams with interesting applications such as subwavelength-resolution imaging devices, metamaterial antennas, negative-index passband filters, waveguides with MTM inclusions for e-m wave manipulation and restoration of evanescent waves. However, MTMs are strongly anisotropic, and realizing the isotropic response of MTMs with simultaneous occurrence of negative $\varepsilon_r$ and $\mu_r$ is quite complex. It is observed that several reported MTM structures [14–17] are sensitive to the polarization state of the incoming e-m waves. However, an optical element with polarization independence is essential for gathering information from far-field sources. To overcome the polarization sensitiveness, some works [18–20] realized NI MTMs with symmetric orthogonal metallic components to enhance the optical coupling. Nevertheless, the functionality is constrained mostly for normal incidences. In reality, however, one cannot expect the incoming rays from distant objects to be always normal to the interface. The deviation from the normal incidence leads to optical aberration, which causes a loss of information. Hence, researchers [21] proposed an MTM that is insensitive to the incoming THz wave's polarization and incident angle.

Moreover, it is noted that the inevitable requirement for isotropic behavior is still not achieved as the MTM unit cell functionalities [22–24] are mostly restricted to 1-D or 2-D patterns. In a few works [25, 26], researchers used the resonance behavior of all dielectrics to attain the 3-D functional NI MTMs. Even though the fabrication of such MTMs is possible and it possesses isotropic behavior, the operational bandwidth is relatively narrow. Also, a few research groups [27, 28] used the conventional way of attaining a negative index in a microwave regime where the unit cells are mainly composed of identical metallic structures printed on all sides of the dielectric cube. However, such combinations are not feasible to extend beyond the microwave region. To resolve such limitations, in this work, we demonstrate a 3-D NI MTM composed of orthogonally oriented cross-bars with arrows on each corner embedded in a dielectric cube with a period of $0.34\lambda$, with a broadband negative index regime under multiple polarizations and incident angles at THz frequencies. The numerical results show that the achieved negative index bandwidth in the proposed 3-D NI MTM is around 0.23 THz, with a bandwidth of 27.15%.

Based on the realized 3-D NI MTM, we design a THz planoconcave lens (PCL), as far-field imaging is imperative for most THz optics applications. A PCL [29] made of a negative index medium is a counterpart of a positive index planoconvex lens, which permits the focusing of far-field radiation [30, 31], and it has the upper hand on reduced aberration. Most previously reported THz meta-lenses [32–35] have either low resolution or small numerical aperture (NA), limiting the far-field imaging application. Using a PCL made of the proposed 3-D NI MTM, we attained the focused spot of far-field radiation for a wide range of incident angles for linear and circular polarization states.

Rest of the manuscript is arranged as follows. Section 2 presents the design and structure of the proposed 3-D NI MTM and its effective parameters. The role of incident angle and polarization dependence on the proposed MTM properties is further investigated in this section. Section 3 establishes the shape and construction of planoconcave lens followed by its far-field focusing characteristics for linearly and circularly polarized waves. Also, the role of the incident angle and radii of curvature of the PCL for the incoming plane waves are shown in this section. Finally, in Section 4, a discussion of the suitable fabrication techniques for the proposed 3-D MTM is presented.

## 2. THE PROPOSED 3-D MTM STRUCTURE AND ITS NEGATIVE INDEX REGIME

The unit cell of the proposed 3-D NI MTM and its simulation setup are shown in Fig. 1. The unit cell of NI MTM is composed of a single layer cross-bar [18] with arrows on each corner oriented in three orthogonal directions with a common center. The metallic bar is made of gold (electrical conductivity $\sigma = 4.561 \times 10^7 \, \mathrm{Sm}^{-1}$) and immersed in a dielectric cube. The cube has a relative dielectric permittivity of $\varepsilon_r = 2.67$. Practically, material such as Benzocyclobutene (BCB) serves as suitable dielectric background material for THz frequencies with this dielectric permittivity [36]. We choose the thickness and width for the metallic bar and its arm as $t = 10 \, \mu\mathrm{m}$ and $w = 10 \, \mu\mathrm{m}$, respectively. The other
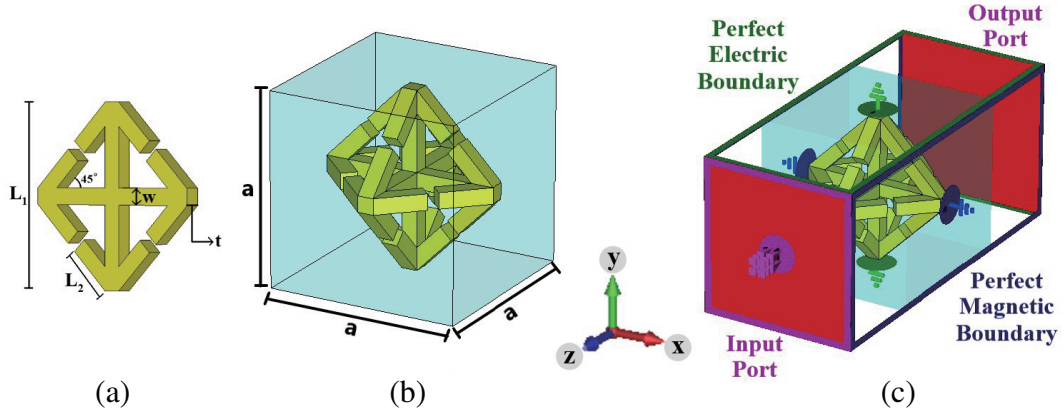
**Figure 1.** Unit cell of a proposed 3-D NI MTM. (a) Cross-sectional view. (b) One complete unit cell. (c) Unit cell simulation setup with fictitious waveguide boundary conditions.

geometric dimensions of the unit cell are the lattice constant $a = 120\,\mu\mathrm{m}$, the bar's length $L_1 = 110\,\mu\mathrm{m}$, and the arrow arm's length $L_2 = 32\,\mu\mathrm{m}$.

The transmission properties of the proposed 3-D NI MTM structure are numerically computed through full-wave e-m simulations using finite-integration based e-m solver CST Studio Suite. In the transmission calculation, unit cell is employed with fictitious waveguide boundary conditions [37]. This means that for a normal incident transverse electric (TE) polarized e-m wave, the two surfaces of the unit cell parallel to the $yoz$ plane, and that parallel to the $xoz$ plane are employed with perfect magnetic $(\hat{n} \times \vec{H} = \vec{0})$ and perfect electric boundary $(\hat{n} \times \vec{E} = \vec{0})$ conditions, respectively as shown in Fig. 1(c). The propagation direction of the incident wave is along the $z$-axis, and the two surfaces of the unit cell parallel to the $xoy$ plane are employed as the input/output excitation ports along with perfectly matched layer (PML) absorbing boundary conditions.

From the extracted complex transmission $(S_{21})$ and reflection $(S_{11})$ coefficients, the effective parameters of the MTM can be obtained using the standard retrieval procedure [37]. The relative wave impedance $(z_r)$ and refractive index $(n)$ in terms of scattering parameters are given by Equations (1)–(2) as follows:

$$z_r = \sqrt{\frac{\mu_r}{\varepsilon_r}} = \frac{1 + \Gamma_{12}}{1 - \Gamma_{12}} \tag{1}$$

$$n = \sqrt{\varepsilon_r \mu_r} = j\frac{c}{2\pi\nu d}\left[\ln|\tau| + j\arg(\tau)\right] \tag{2}$$

where $d$ is the thickness of the medium, $\nu$ the corresponding frequency, $c$ the velocity of light in free space, and $\tau$ and $\Gamma_{12}$ are expressed as,

$$\tau = \frac{(S_{11} + S_{21}) - \Gamma_{12}}{1 - (S_{11} + S_{21})\,\Gamma_{12}} \tag{3}$$

$$\Gamma_{12} = \frac{1 - \left(S_{21}^2 - S_{11}^2\right)}{2S_{11}} \pm \sqrt{\left[\frac{1 - \left(S_{21}^2 - S_{11}^2\right)}{S_{11}}\right]^2 - 1} \tag{4}$$

By combining Equations (1) and (2), the effective material parameters such as relative dielectric permittivity $(\varepsilon_r' - j\varepsilon_r'')$, relative magnetic permeability $(\mu_r' - j\mu_r'')$, and refractive index $(n_r' - jn_r'')$ can be retrieved.

Figure 2(a) shows the transmission $(S_{21})$ and reflection $(S_{11})$ coefficients of a single 3-D NI MTM unit cell with thickness of $120\,\mu\mathrm{m}$. Using Equations (1)–(4) mentioned above, the effective parameters of the proposed 3-D structure are extracted and plotted in Figs. 2(b)–2(d). It is observed that the real parts of the effective permittivity (Fig. 2(b)) and permeability (Fig. 2(c)) simultaneously drop from positive to negative around 0.75 THz. The general condition for the negative refraction $\varepsilon_r' < 0;\ \mu_r' < 0$
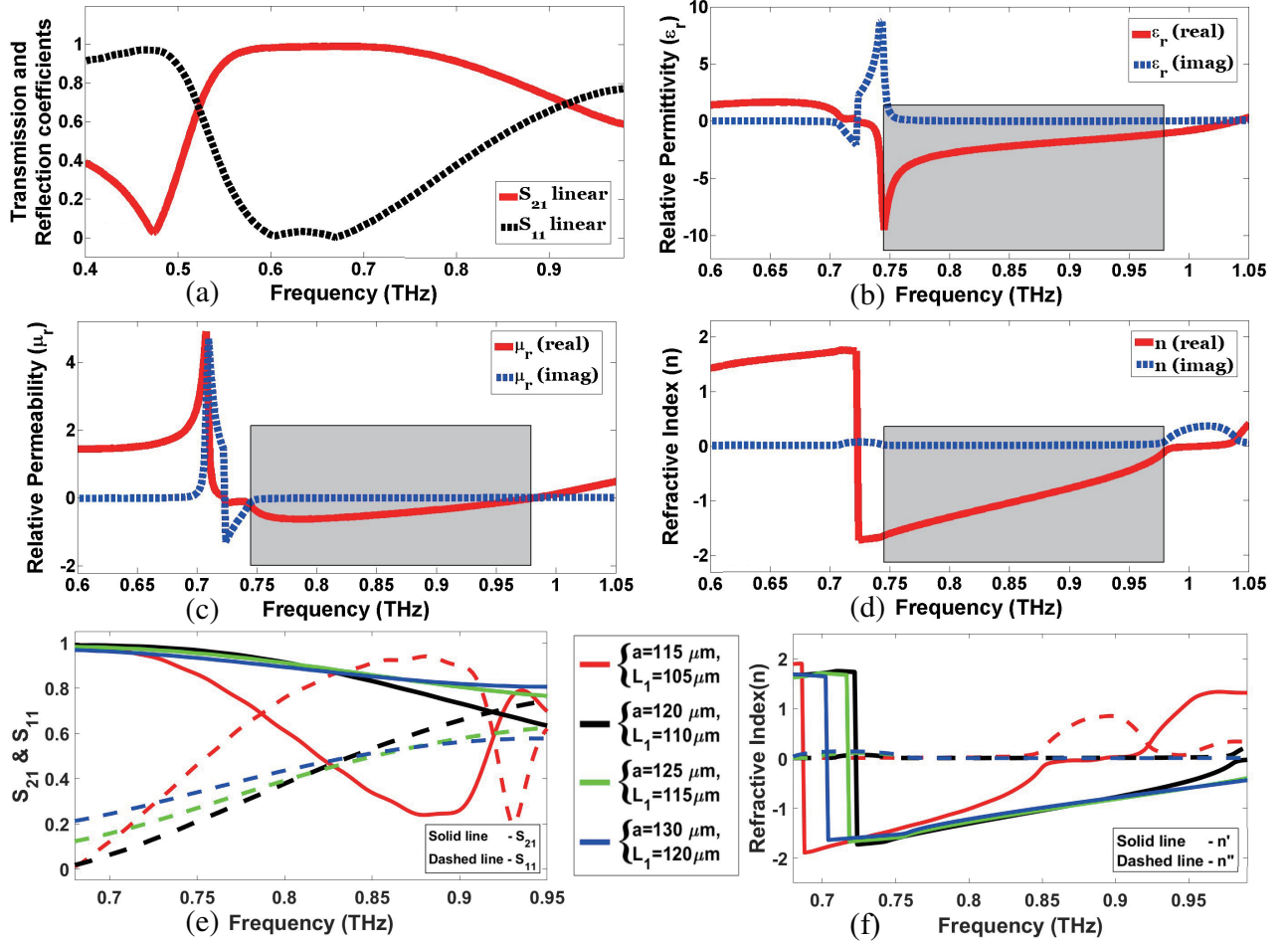
**Figure 2.** (a) Transmission ($S_{21}$) and reflection ($S_{11}$) coefficients of the 3-D NI MTM. Real and imaginary parts of (b) relative dielectric permittivity, (c) relative magnetic permeability, and (d) refractive index of the 3-D NI MTM. The NI range is shaded between 0.745 THz to 0.979 THz. Scalability of the unit cell by varying its lattice constant ($a$) and length of metallic bars ($L_1$): (e) Transmission and reflection coefficients and (f) real and imaginary parts of refractive index of the 3-D NI MTM for different dimensions.

is satisfied in the frequency band between 0.745 THz and 0.979 THz, with the operational bandwidth of 0.234 THz (27.15%). Especially when the value of refractive index is $n = -1$, at 0.85 THz, the power flows calculated with and without MTM unit cell are found to be $5.13 \times 10^7 \text{W/m}^2$ and $6.8 \times 10^7 \text{W/m}^2$, respectively. This shows the high transmission behavior of the proposed 3-D NI MTM. It may be noted that the achieved negative index bandwidth is sufficient for the practical THz device realizations.

The operational frequency mainly depends on the length of the cross-bar components which results in the scalability of the unit cell for the desired frequency regimes. The effects of length of the metallic bars ($L_1$) and lattice constants ($a$) on the scattering parameters and refractive index of the 3-D MTM are shown in Figs. 2(e) and 2(f), respectively. Since the frequencies below 1 THz are of particular interest for THz devices, the unit cell dimensions are chosen as shown in Fig. 1. It is also important to note that the extracted parameters of the MTM are similar when the Drude model for gold is used, as the operating frequency range is within 1 THz.

To understand the existence of NI behavior of the proposed 3-D NI MTM structure, surface current pictures are presented. Generally, for any MTMs, a NI regime exists when the structure exhibits electric and magnetic resonances in the same frequency band. The electric resonance in the proposed 3-D NI

MTM is mainly excited by the cross-bar component (Fig. 1(a)) parallel to the incident electric field direction. The cross-bars form an array of small electric dipoles, thus leading to a negative effective permittivity due to the stimulated oscillations of the conducting electrons for e-m waves exciting the NI MTM structure. Similarly, together with the capacitive gap formed between the arms of two neighboring arrows (Fig. 1(b)), the unit cell may be considered as an LC circuit in which the inductance is expected to build in the loop formed between the bars and arms of opposite arrows of the 3-D NI MTM unit cell. Therefore, under e-m wave excitation, a magnetic field component perpendicular to the area between the crosses and the arrows induces a current flowing in the metallic structure.

Thus, the magnetic resonance in the proposed 3-D unit cell is mainly caused by the induced multiple current loops, similar to the split-ring resonator. To show the presence of electric and magnetic resonances in the proposed structure, surface current is presented for TE and TM wave excitations at 0.85 THz in Figs. 3(a) and 3(b), respectively. The black arrows represent the direction of the electric dipole moment in the MTM. The anti-symmetrically oriented electric dipoles show a
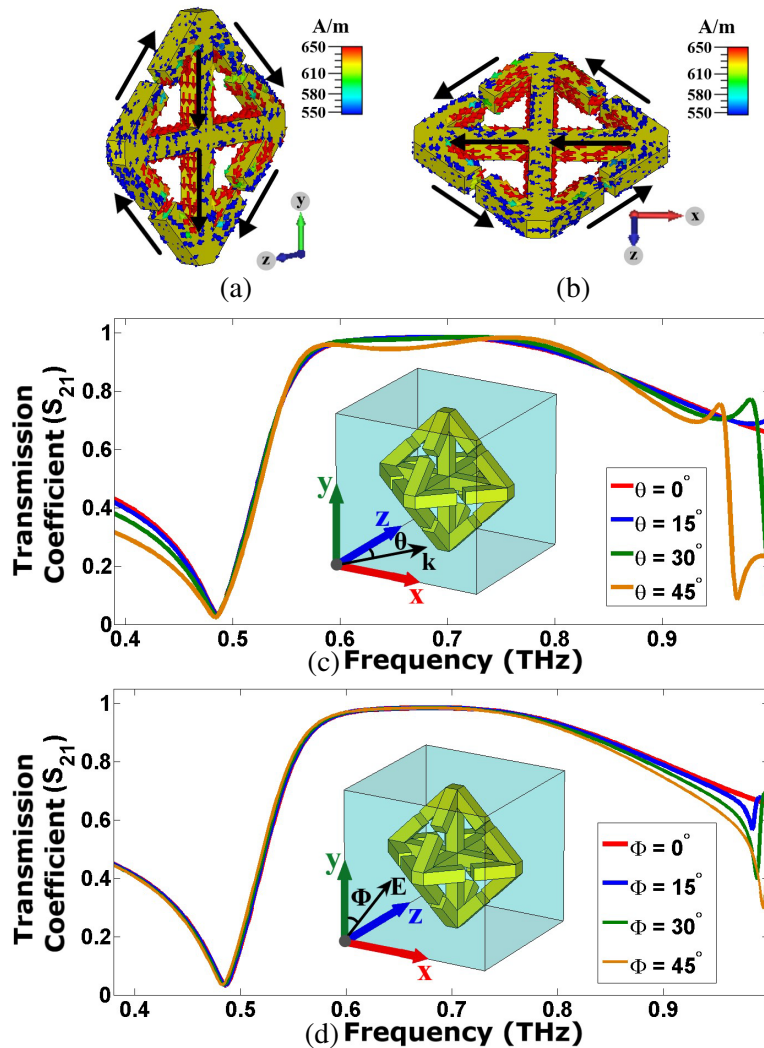


**Figure 3.** (a) and (b) Cross-sectional view of surface current distributions in *yoz*- and *xoz*-planes at 0.85 THz for TE and TM wave excitations, respectively. Transmission coefficients (c) for variation in incident angle from 0° to 45° (Inset shows the schematic used for the incident angle variation) and (d) for variation in polarization angle from 0° to 45° (Inset shows the schematic used for the polarization angle variation).

non-zero net magnetic dipole moment. Since anti-parallel oscillations of electric dipoles constitute a magnetic dipole, one would expect magnetic resonance in the proposed 3-D unit cell for both TE and TM excitations. Moreover, the symmetry of the proposed 3-D pattern indicates that MTM exhibits both electrical/magnetic resonances for e-m waves with any polarizations and non-normal incidences.

The incident and polarization angle dependency of the proposed MTM can be calculated by employing the unit cell structure with input/output excitation ports along $z$ directions with perfectly matched layers (PML) and with unit cell boundary conditions along $x$ and $y$ directions. To analyze the wide-angle functionalities of the 3-D NI MTM with the proposed unit cell, the effects of exciting planewaves with oblique incidences are studied. For oblique incidence cases, it is sufficient to consider the incidence angle ($\theta$) variation $0°$ to $45°$ due to the symmetry of the proposed unit cell. Fig. 3(c) shows the transmission coefficient of a 3-D unit cell for incident angle variation under TE mode excitation. It is found that the transmission characteristics are quite insensitive to the incident angle variations over a wide negative index regime.

Similarly, to verify the polarization sensitiveness for the proposed 3-D NI MTM, the polarization angle ($\Psi$) of the incident e-m wave is changed from $0°$ to $45°$, and the transmission coefficient is plotted in Fig. 3(d). It is observed that within the negative refraction band, the 3-D NI MTM unit cell's transmission characteristics are insensitive to the change of polarization angle. Thus, the proposed 3-D MTM is insensitive to both polarizations and incident angle of the e-m wave at least up to $45°$ due to the symmetry of the MTM. Moreover, it is also verified that the retrieved parameters are independent along all three principal axes ($x$, $y$, $z$) of the MTM under normal incidences. Hence, one can claim the isotropy nature of the designed unit cell at least along the principal axes of the MTM.

## 3. PLANOCONCAVE LENS BASED ON 3-D NI MTM STACK

Lenses with a shorter focal length [38] are helpful for high optical power requirements in light-matter interactions. A convex lens made with double positive (DPS) material would focus parallel rays from a source at a distant location. However, for a shorter focal length, the lens material must have a higher index of refraction. In such lenses, most of the incident rays would be reflected back; hence, very little of the incident beam would be transmitted. Suppose that we employ a lens with a negative index of refraction, we can relax the requirement of high refractive index values, because a NI MTM lens shows more significant bending of the incident waves even for the moderate value of the negative index. At the same time, one may note that an MTM slab [29, 39] with a negative index of refraction will not be helpful for far-field focusing of e-m radiation.

The design of a PCL with a negative index of refraction is a potential candidate for achieving shorter focal length elements. As shown in Fig. 4(a), the incoming parallel rays are bent on the same side of the normal (dashed line NM in Fig. 4(a)) at the points of incidence on the curved surface due to the negative refraction. Hence, the incoming planewaves are expected to converge to a focal point (F) closer to the lens, resulting in a shorter focal length than a conventional positive index convex lens. In this work, we built a PCL using the proposed 3-D NI MTM structure, as shown in Fig. 4(b). Initially, we designed a slab with eleven-unit cells along each transversal direction (along $x$ and $y$ axes) and six layers along the propagation direction. Then, by removing one unit cell step by step, starting from the back side of the slab along the transversal section of each layer, a PCL profile is achieved, as shown in the cross-sectional view (Fig. 4(c)). This scheme represents a staircase approximation of an ideal parabola. It is expected that the designed PCL can attain 3-D focusing for the incoming e-m waves due to the high degree of symmetry of the MTM unit cell.

Here, the PCL's base layer thickness ($2a$) and aperture size ($11a \times 11a$) are chosen so that a well-defined focal spot is observed for different polarizations, angles of incidence, and radii of curvature. Full-wave e-m simulations for the designed PCL are done with the transient solver using CST Studio Suite. As shown in Fig. 4(d), the computation of the finite PCL geometry involves open PML boundary conditions along all directions, and normal incident planewave with TE/TM polarizations, left-circularly polarized (LCP) and right-circularly polarized (RCP) waves are excited at 0.85 THz (corresponds to the NI regime (i.e., $n \approx -1$) of the 3-D NI MTM). To minimize the reflection from walls of the computational domains, one can use (i) scattering and (ii) perfectly matched layer (PML) boundary conditions (BCs). Scattering boundary conditions are ideal for normal incident light, but they will not effectively minimize
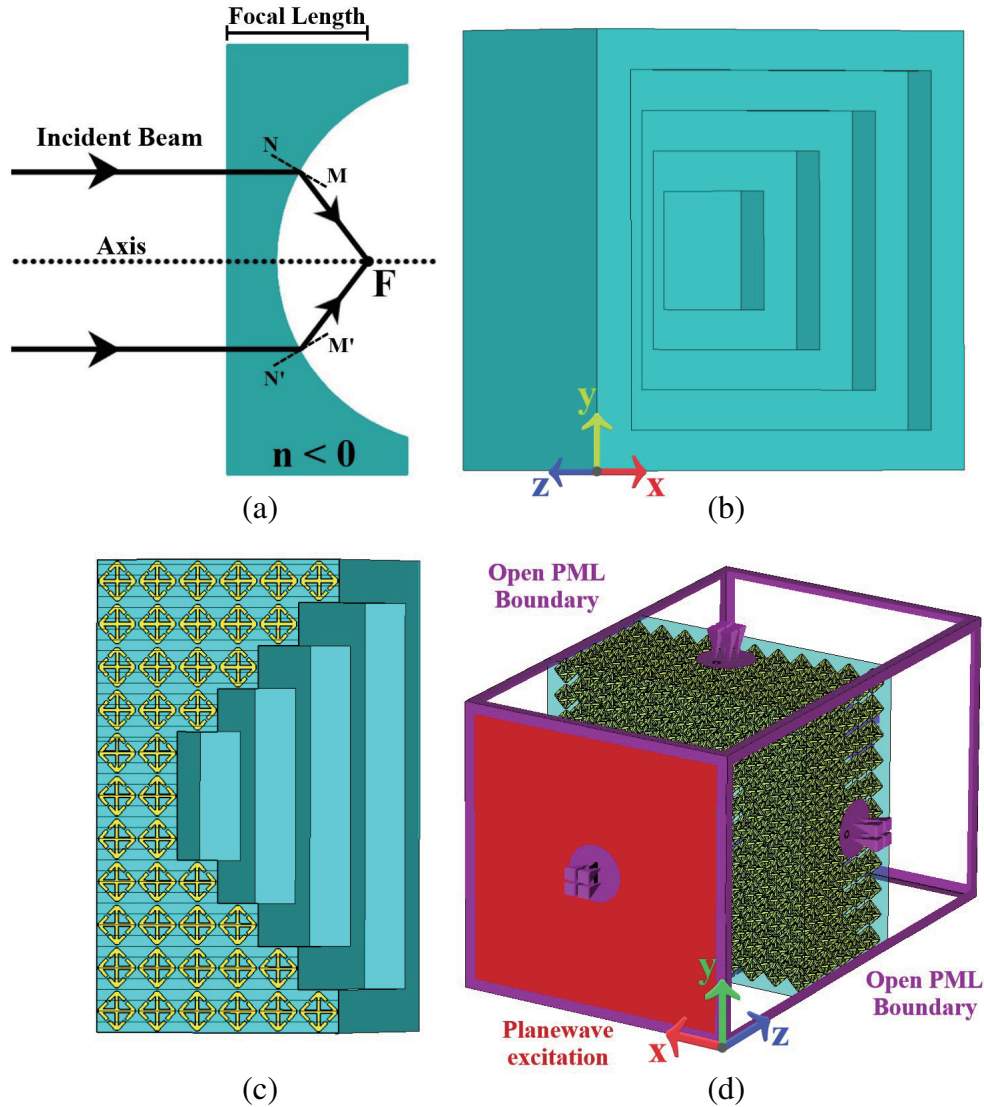
**Figure 4.** (a) Refraction in PCL with negative index. (b) PCL design with 3-D NI MTM unit cells. (c) Cross-sectional view of the parabolic PCL profile based on staircase approximation. (d) PCL simulation setup with PML boundary conditions.

reflection due to oblique incident rays. On the other hand, PML BCs are absorbing layers suitable to nullify reflection from the boundary walls irrespective of the incident angle, polarization, and frequency of the scattered waves. These are the main advantages of PML BCs over scattering and periodic BCs. At the same time, the thickness of the PML layers is important in the computational calculations. In our work, we employed PML layers of thickness $4\lambda$.

## 3.1. PCL Focusing for Linearly Polarized Waves

Figures 5 and 6 show the electric and magnetic field norm distributions in the PCL configuration for a normal incident $y$-polarized (TE) and $x$-polarized (TM) waves, respectively, at 0.85 THz. It is evident that the PCL shows focusing functionality for all three planes and thus ensures 3-D focusing functionality. The bright spots concentrated at the back side of the PCL show that it behaves as a converging lens for the incoming planewaves. The foci observed for both fields are very close to the parabolic surface. Moreover, the electric field distributions shown for the $xoz$ plane (Fig. 5(b))
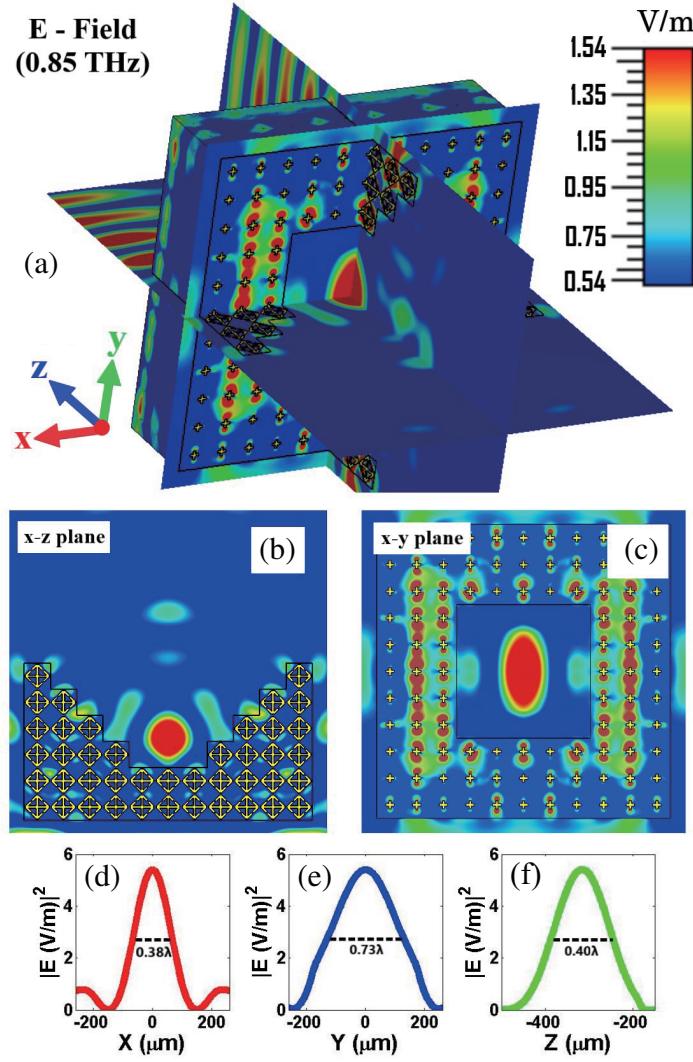
**Figure 5.** (a) Electric field norm distribution shows 3-D focusing of a PCL excited with TE planewaves at 0.85 THz. Electric field norm distribution along (b) the $xoz$ plane (c) the $xoy$ plane are shown. Transverse scanning intensity profile of the focused spot along (d) $x$-axis, (e) $y$-axis, (f) $z$-axis, and its calculated FWHMs are $0.38\lambda$, $0.73\lambda$ and $0.40\lambda$ respectively at 0.85 THz. The back focal length of the PCL is $F = 3.16a$ for a TE wave at 0.85 THz.

and $xoy$ plane (Fig. 5(c)) reveal strong focusing spots, but the spot size is asymmetric. To affirm the asymmetry of the focusing spots, intensity profiles are scanned along the transverse direction, as plotted in Figs. 5(d)–5(f).

The full-width half-maximum (FWHM) computed for intensity profiles represents the spot size of the focused beam. For electric field intensity distribution, the computed spot sizes are $0.38\lambda$, $0.73\lambda$ and $0.40\lambda$ along $x$-, $y$-, and $z$-axes, respectively, under normal incident $y$-polarized TE wave at 0.85 THz. It is noted that the focused spot is elongated along the polarization direction of the incoming e-m waves, and it is attributed to the step-by-step staircase approximation of the parabolic-concave profile.

In addition, the simulated focusing efficiency of 64.4% is obtained for the designed PCL. The focusing efficiency is calculated as the ratio of the optical intensity in the focal plane (with a spanning area of $2\text{FWHM}_x \times 2\text{FWHM}_y$, where $\text{FWHM}_x$ and $\text{FWHM}_y$ are FWHMs calculated along $x$- and $y$-axes of the focused spot, respectively) to that of the incident beam. The incident beam is defined as the optical intensity passing through an aperture with the same dimensions as the MTM lens. Similarly,
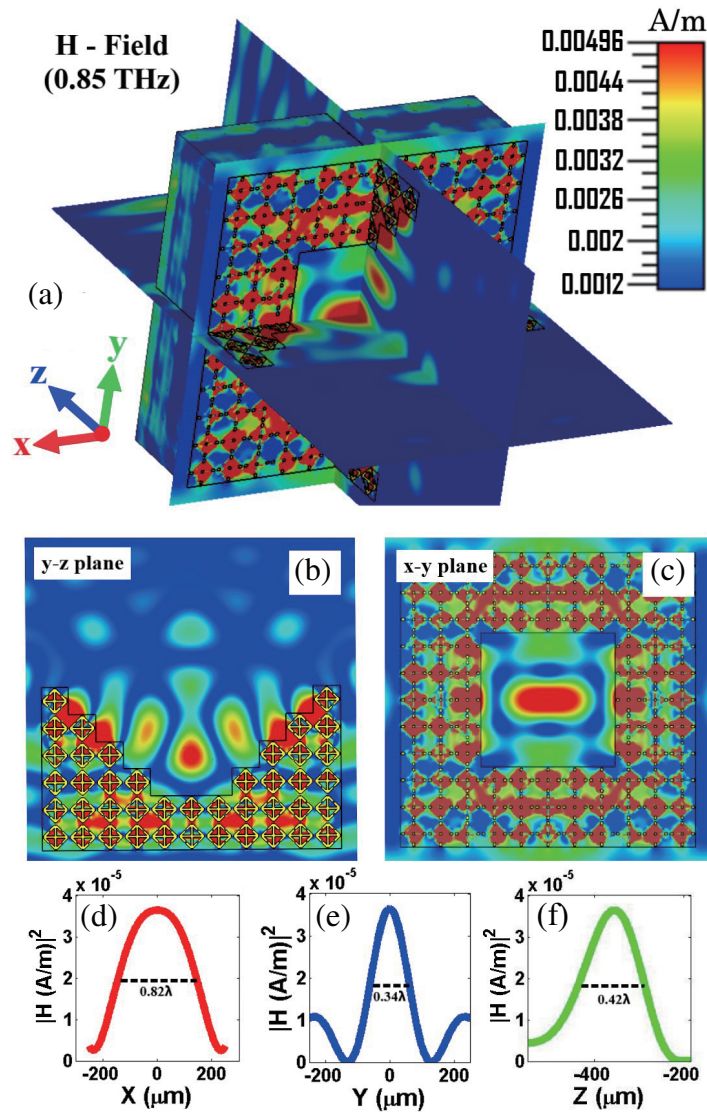
**Figure 6.** (a) Magnetic field norm distribution of a PCL excited with TM planewaves at 0.85 THz. Magnetic field norm distribution along (b) the $yoz$ plane (c) the $xoy$ plane are shown. Transverse scanning intensity profile of the focused spot along (d) $x$-axis, (e) $y$-axis, and (f) $z$-axis and their calculated FWHMs, which are $0.82\lambda$, $0.34\lambda$, and $0.42\lambda$, respectively. The back focal length of the PCL is $F = 3.46a$ at 0.85 THz.

for magnetic field distribution shown in Figs. 6(a)–6(c), the computed spot sizes are $0.82\lambda$, $0.34\lambda$ and $0.42\lambda$ along $x$-, $y$-, and $z$-axes, respectively, under normal incident $x$-polarized TM wave at 0.85 THz. The size of the focal spot signifies that sub-wavelength focusing is achieved along the two directions perpendicular to the polarization direction of the incoming planewaves. It is clear that, in both cases, the focal depth (spot size calculated along the propagation direction) is also in sub-wavelength dimensions. The back focal lengths calculated from electric and magnetic field norm distributions are found to be $3.16a$ ($1.07\lambda$) and $3.46a$ ($1.18\lambda$), respectively, where $a$ is the lattice constant, and $\lambda$ is the corresponding wavelength. It is helpful to note that here the back focal length of a PCL is calculated from the incident point of the PCL to the focusing spot rather than center of the PCL.

It is essential to emphasize that though the proposed 3-D MTM exhibits negative index for all polarizations, different dielectric response ($\varepsilon_r = -2.19 - j0.008$ at 0.85 THz) and magnetic response ($\mu_r = -0.49 - j0.005$ at 0.85 THz) of MTM unit cell inevitably result in asymmetric focusing spot size

and difference in focal lengths for electric and magnetic fields.

We also verify the focusing behavior of the PCL configuration for LCP/RCP waves, as imaging with circular polarization functionality may lead to the development of polarization contrast imaging at THz waveband.

## 3.2. PCL Focusing for Circularly Polarized Waves

Figure 7 shows the electric field norm distributions in the proposed PCL and the transverse scanning intensity profiles for LCP and RCP plane-wave excitations, respectively. The transverse profiles of electric field intensities are taken along three mutually perpendicular lines passing through the focal points for both polarizations.
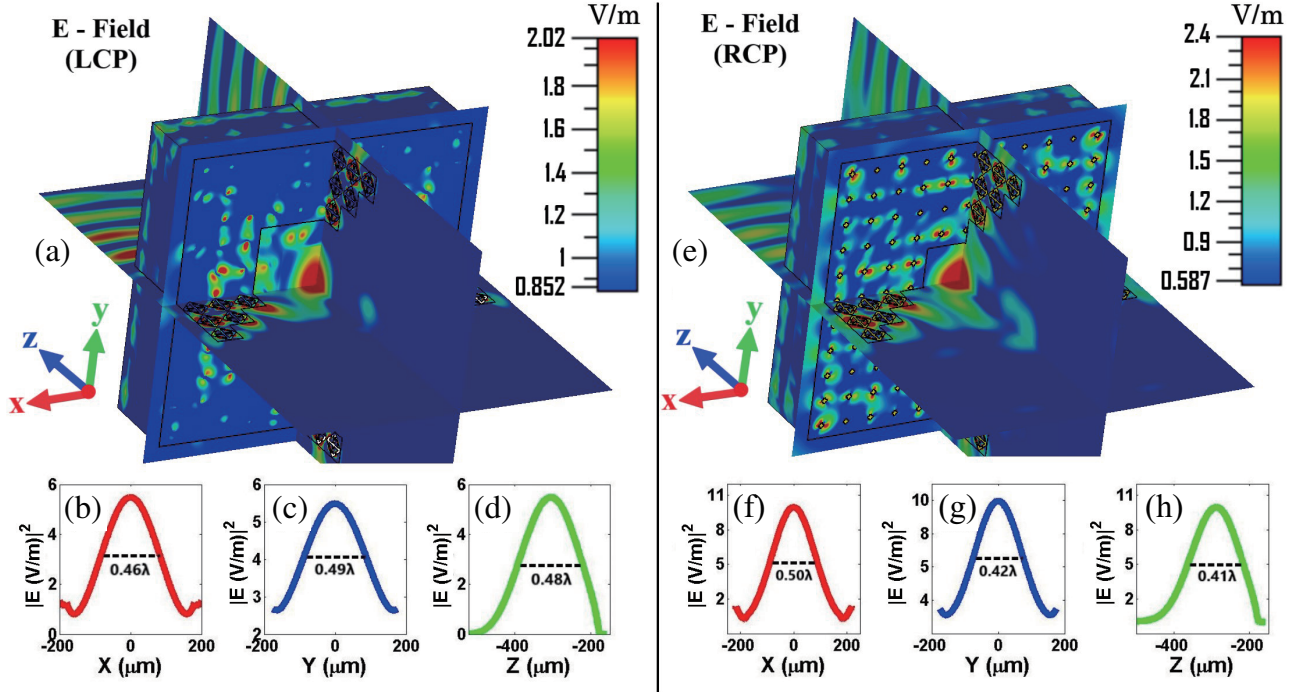


**Figure 7.** (a)–(d) ((e)–(f)) Electric field norm distribution showing 3-D focusing and calculated FWHMs from the transverse profiles taken along $x$-, $y$- and $z$-axes when the PCL is excited with LCP (RCP) respectively at 0.85 THz. The back focal lengths of PCL are $F_{LCP} = 3.04a$ and $F_{RCP} = 2.89a$ at 0.85 THz.

The computed spot sizes are $0.46\lambda\,(x)\times0.49\lambda\,(y)\times0.48\lambda\,(z)$ for LCP wave and $0.50\lambda\,(x)\times0.42\lambda\,(y)\times0.41\lambda\,(z)$ for RCP wave, respectively, which represent the 3-D focusing with sub-wavelength features of the PCL for the circularly polarized waves. The back focal lengths of the PCL lens computed for the LCP and RCP waves are $3.04a\,(1.03\lambda)$ and $2.89a\,(0.98\lambda)$, respectively, and they are comparatively smaller than the conventional positive index lens. The shorter focal length indicates that the focal point is falling on the extreme near-field region of the PCL, and it is independent of the polarization of the incoming planewaves.

## 3.3. PCL Focusing under Oblique Incidences

To investigate the focusing performance of the designed PCL for oblique incident waves, the incoming TE waves are excited with four different incident angles (i.e., 5°, 10°, 15°, and 20°) at 0.85 THz. The electric field norm distributions and transverse scanning intensity profiles of the spot size are shown in Figs. 8(a)–(d) and (e)–(f), respectively for various incident angles. The computed FWHM of spot sizes
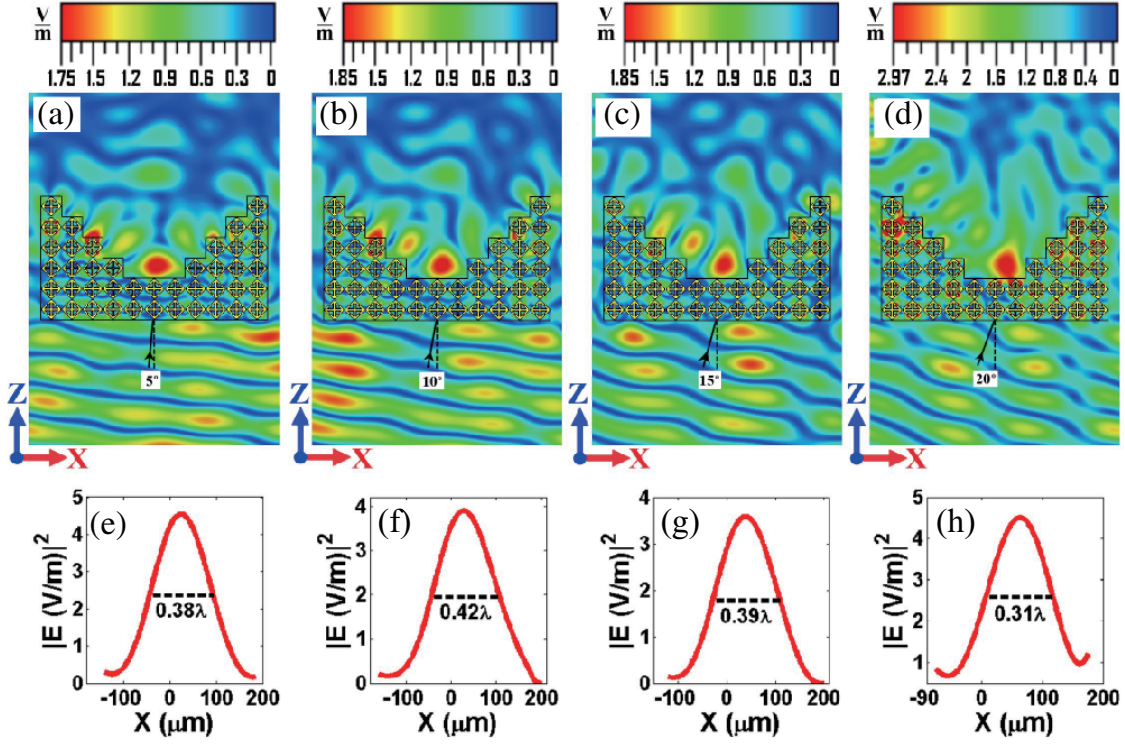
**Figure 8.** (a)–(d) Electric field norm distribution showing focusing by PCL and (e)–(h) Electric field intensity profiles scanned along the $x$-axis at the center of the focused spot size for an incident TE wave with four different angles of incidence 5°–20° (in steps of 5°) at 0.85 THz, respectively.

indicates that the proposed PCL exhibits sub-wavelength focusing even for the incident angle variation from 0° to 20°.

Since the incoming rays do not coincide with the PCL's optical axis, the incoming rays refract at different angles at the parabolic interface. For an increase in every five degrees of incident angles, it is observed that there is a transversal shift (perpendicular to the $z$-axis) of a focal point. Further increase in incident angle ($\theta > 20°$) results in deformation of the focusing spot due to the finite light collection area of the PCL. It is evident that the proposed PCL is independent of incident angle limited to the curvature of the parabolic profile, showing far-field focusing not only for normal incidence but also for oblique incidences.

### 3.4. PCL Focusing with Different Radius of Curvatures

Finally, to analyze the effect of curvature of the PCL profile, another approximated parabolic profile is designed with larger radius of curvature. Here, a flat slab is stacked with 11-unit cells along each transversal direction (along $x$ and $y$ axes) and 4-layers along propagation direction (along $z$ axis). Then, 5-unit cells and 7-unit cells are removed from the third and fourth layers of the slabs, respectively, along its each transversal direction. The two parabolic profiles are stacked for a different radius of curvature $R_1 = 4.75a$ and $R_2 = 5.8a$ as shown in Figs. 9(a) and (b), respectively, and excited with plane waves along $z$ direction at 0.85 THz by keeping open PML boundary conditions along all other directions. Due to the increase in curvature radius, it is expected that the focal point will be axially shifted away from the lens. To investigate the shift of focal point, normal incident TE waves are impinged on the two different profiles. The electric field distributions along the focal plane are shown in Figs. 9(c) and (d) corresponding to $R_1$ and $R_2$ which respectively signify a lateral shift on the focusing spot along the axial direction.

Moreover, the decrease in numerical aperture (NA) shows a significant drop in the resolution of the
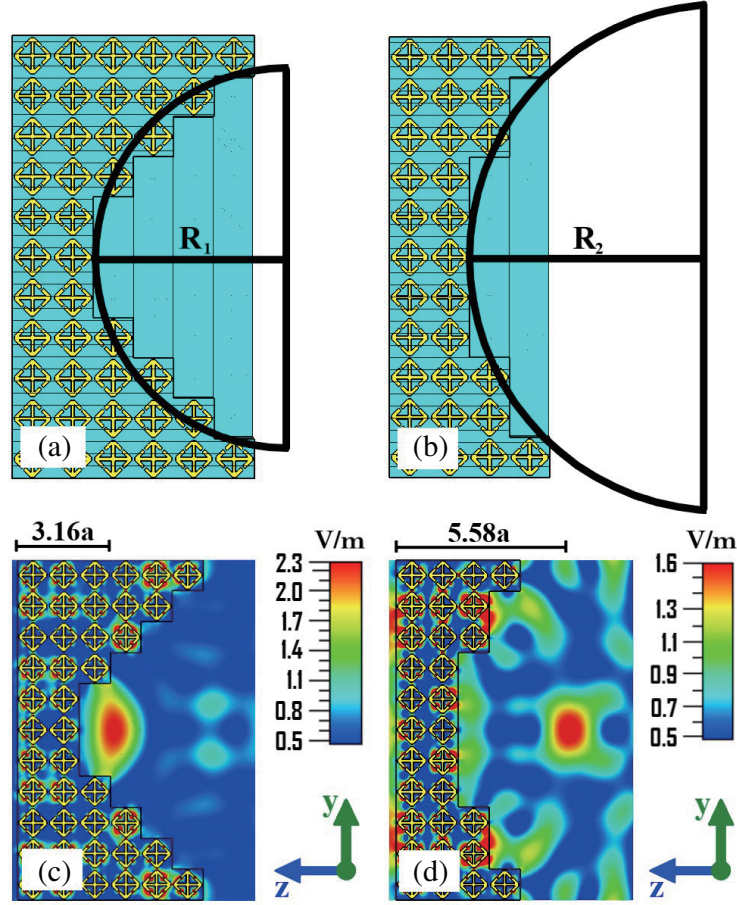
**Figure 9.** (a) and (b) PCLs with two different radii of curvature $R_1 = 4.75a$ and $R_2 = 5.8a$, respectively. (c) and (d) The electric field maps show the change in focal spots for different parabolic profiles. The observed back focal lengths are $F_1 = 3.16a$ and $F_2 = 5.58a$ for radii $R_1$ and $R_2$, respectively.

image formed. The intensity of the focal point drops for the lowered NA profile, which signifies that the focusing efficiency of the low NA profile is low. However, it is observed that the NA of the designed PCL is high enough to get the focal spot near the lens surface, and the alteration in curvature leads to the shift in the focal position.

    Thus through the numerical analysis, the following aspects are observed in this work: (i) the proposed unit-cell structure is 3-D symmetric with a wide NI regime at THz frequencies; (ii) the designed PCL focuses the incoming planewaves in the extreme near-field region with minimal losses; (iii) the designed PCL is polarization insensitive; (iv) the spot sizes are calculated to be in sub-wavelength range with reduced aberration; (v) focusing is achievable for oblique incidence; and (vi) lateral shift of focus is observed by reducing the numerical aperture. For instance, Table 1 compares the significant results of the present work with respect to the existing references.

    From the first aspect, it is clear that the behavior of the proposed 3-D NI MTM is independent of the incident direction, and hence the functionality is the same in all three principal directions. The second aspect points out that focusing can be achievable with PCL made of NI materials, and it is a counterpart of convex lens made of double positive index material. Moreover, in the case of NI MTM, focusing occurs in the region near the lens, which cannot be achieved even with conventional lenses of a very high refractive index. The third aspect conveys that the 3-D focusing behavior of the PCL is independent of the polarization (TE, TM, LCP, or RCP) of the incoming planewaves. The fourth aspect reveals that the resolution of the proposed PCL is high, which also transmits most of the incoming waves.

**Table 1.** Comparison with previously reported MTM-based far-field focusing lenses [UCF — Unit Cell Functionality, FL — Focal Length, FWHM — Full Width at Half Maximum (Spot Size), FD — Focal Depth].

| | References | UCF | FL | FWHM | FD | Polarization | $\lambda$ |
|---|---|---|---|---|---|---|---|
| [40] | Hashemi et al. (2016) | 1D | $\sim 7\lambda$ | $>0.5\lambda$ | - | Linear (cross) | $476\,\mu m$ |
| [41] | Mendis et al. (2016) | 2D | $\sim 20\lambda$ | $\sim 2.3\lambda$ | - | Linear | $1764\,\mu m$ |
| [42] | Jia et al. (2017) | 1D | $\sim 292\lambda$ | $\sim 6.6\lambda$ | $\sim 78\lambda$ | Sensitive | $96\,\mu m$ |
| [43] | Zhang et al. (2017) | 1D | $\sim 20\lambda$ | $\sim 1.6\lambda$ | $>30\lambda$ | Linear | $299\,\mu m$ |
| [44] | Chen et al. (2018) | 1D | $\sim 100\lambda$ | $\sim 0.46\lambda$ | - | Insensitive | $119\,\mu m$ |
| [45] | Jiang et al. (2018) | 1D | $\sim 300\lambda$ | $\sim 1.1\lambda$ | $\sim 1.2\lambda$ | Insensitive | $119\,\mu m$ |
| [46] | Cheng et al. (2019) | 1D | $\sim 24\lambda$ | $\sim 1.3\lambda$ | $>6\lambda$ | Insensitive | $499\,\mu m$ |
| [47] | Zang et al. (2019) | 1D | $\sim 32\lambda$ | $\sim 2.3\lambda$ | $\sim 23\lambda$ | Insensitive | $434\,\mu m$ |
| | **This work** | **3D** | $\sim\lambda$ | $\sim 0.38\lambda$ | $\sim 0.4\lambda$ | **Insensitive** | $\mathbf{353\,\mu m}$ |

The fifth aspect signifies that PCL converges the parallel rays not only for normal incidence but also for oblique incidence, subject to the limitations of parabolic profile. The last and sixth aspects ensure that by lowering the numerical aperture by increasing the curvature radius, the focal point is axially shifted away from the surface. It resembles that designed PCL has a high numerical aperture which focuses the incoming rays very close to it with minimal losses. Even though the proposed PCL has an approximated parabolic profile, various aspects of focusing parallel rays are achieved. By reducing the approximations to the parabolic profile, the focusing characteristics of the proposed PCL can be enhanced.

## 4. FEASIBLE FABRICATION TECHNIQUES

Though 3-D MTM with NI is warranted for practical applications, realizing 3-D geometries is not an easy task. However, recently several 3-D MTM geometries are successfully fabricated due to the advent of advanced fabrication techniques. For example, multiphoton microfabrication [48], direct laser writing (DLW) [49], mask-directed micro-3D printing [50], focused-ion-beam (FIB)-stress induced deformation (SID) [FIB-SID] method [51], and super-fine-ink-jet (SIJ) printing [52] can be used to manufacture 3-D MTM geometries.

Multiphoton microfabrication technique uses DLW with a femtosecond pulsed laser beam to fabricate 3-D microstructures with very high resolution up to submicron level. An ideal tool for microfabrication is FIB-SID which utilizes induced surface stress to bend the cantilever upward or downward to construct various 3-D optical micro and nanostructures with flexible and complex geometry. In this technique, hybrid fabrication with the combination of 3-D printing, metal coating, and wet etching has been proposed to fabricate the 3-D ring MTM geometries with high accuracy. Currently, mask-directed multiphoton lithography (MDML) based micro-3D printing ($\mu$-3DP) is used for fabricating complex 3-D prototypes assisted by computer-aided design (CAD). In this approach, unique and predictable features could be generated using masks that act as projection tools for the fabrication of geometries in traditional photolithography.

These techniques have the greatest potential to manufacture three-dimensional microscale and structurally complex metamaterials as it provides intrinsic submicron resolution for 3D structures. Recent experimental works based on THz MTMs [49, 51, 53, 54] also show that the fabrication of complex geometries is possible in micro and nanostructures. Therefore, we anticipate that the proposed 3-D MTM geometry can be fabricated successfully.

## 5. CONCLUSIONS

To conclude, we proposed a 3-D negative refractive index MTM at THz frequencies, with a negative refractive bandwidth of 0.234 THz (relative value 27.15%). The transmission spectra and retrieved effective material parameters verify the negative index properties of the 3D NI MTM. A PCL has been designed based on the proposed 3D NI MTM using a staircase approximation of the ideal parabolic profile. The electric and magnetic field intensity distributions revealed bright focusing spots for the incoming planewaves with different polarizations (TE, TM, LCP, and RCP). Far-field 3-D focusing is realized by the PCL, which also shows sub-wavelength focusing ($< 0.5\lambda$) along at least two principal axes. Focusing by the PCL for different angles of incidences is observed. The observed focal points are in the extreme near-field region ($\sim \lambda$) of the parabolic surface, and it also has a resolution higher than that of a conventional positive index lens. The lowered numerical aperture profile showed a shifting of focal position, which signifies that the designed profile has a high numerical aperture with high focusing efficiency. These results confirm that the far-field focusing by MTM is realizable at higher frequencies, which opens the door for several applications of lenses and imagers in THz optics. Owing to the practical realization 3-D MTM, the fabrication aspects were highlighted.

## ACKNOWLEDGMENT

## DISCLOSURE

The authors declare no conflicts of interest.

## DATA AVAILABILITY

Data underlying the results presented in this paper may be obtained from the authors upon reasonable request.

## REFERENCES

1. Zhang, X. C., "Terahertz wave imaging: horizons and hurdles," *Phys. Med. Biol.*, Vol. 47, No. 21, 3667–3677, 2002.
2. Withayachumnankul, W. and D. Abbott, "Metamaterials in the terahertz regime," *IEEE Photonics Journal*, Vol. 1, No. 2, 99–118, 2009.
3. Parrott, E. P. J., Y. Sun, and E. P. MacPherson, "Terahertz spectroscopy: Its future role in medical diagnoses," *J. Mol. Struct.*, Vol. 1006, No. 1–3, 66–76, 2011.
4. Hu, B. B. and M. C. Nuss, "Imaging with terahertz waves," *Opt. Lett.*, Vol. 20, No. 16, 1716–1718, 1995.
5. Zimdars, D., J. A. Valdmanis, J. S. White, G. Stuk, S. Williamson, W. P. Winfree, and E. I. Madaras, "Technology and applications of terahertz imaging non-destructive examination: Inspection of space shuttle sprayed on foam insulation," *AIP Conf. Proc.*, Vol. 760, 570–577, 2005.
6. Khorasaninejad, M., W. T. Chen, R. C. Devlin, J. Oh, A. Y. Zhu, and F. Capasso, "Metalenses at visible wavelengths: Diffraction-limited focusing and subwavelength resolution imaging," *Science*, Vol. 352, No. 6290, 1190–1194, 2016.
7. Okatani, T., Y. Sunada, K. Hane, and Y. Kanamori, "Terahertz 3D bulk metamaterials with randomly dispersed split-ring resonators," *Nanophotonics*, Vol. 11, No. 9, 2065–2074, 2022.
8. Alex-Amor, A., A. Palomares-Caballero, and C. Molero, "3-D metamaterials: Trends on applied designs, computational methods and fabrication techniques," *Electronics (MDPI)*, Vol. 1, 0, 2022.

9. De Oliveira, J. J., L. D. Ribeiro, E. J. da Silva, R. M. de Souza Batalha, "Design of a free space metamaterial lens based on LC parameters at S-band," *Journal of Electromagnetic Waves and Applications*, Vol. 35, No. 16, 2210–2223, 2021.

10. Veselago, V. G., "The electrodynamics of substances with simultaneously negative values of $\varepsilon$ and $\mu$," *Sov. Phys. Usp.*, Vol. 10, 509, 1968.

11. Grbic, A. and G. V. Eleftheriades, "An isotropic three-dimensional negative-refractive-index transmission-line metamaterial," *J. Appl. Phys.*, Vol. 98, 043106, 2005.

12. Pendry, J. B., A. J. Holden, D. J. Robbins, and W. J. Stewart, "Extremely low frequency plasmons in metallic mesostructures," *J. Phys. Condens. Lett.*, Vol. 10, 4785–4809, 1998.

13. Pendry, J. B., A. J. Holden, D. J. Robbins, and W. J. Stewart, "Magnetism from conductors and enhanced nonlinear phenomena," *IEEE Trans. Microwave Theory Tech.*, Vol. 47, 2075–2084, 1999.

14. Suzuki, T., M. Sekiya, T. Sato, and Y. Takebayashi, "Negative refractive index metamaterial with high transmission, low reflection, and low loss in the terahertz waveband," *Optics Express*, Vol. 26, No. 7, 8314–8324, 2018.

15. Gundogdu, T. F., N. Katsarakis, M. Kafesaki, R. S. Penciu, G. Konstantinidis, A. Kostopoulos, E. N. Economou, and C. M. Soukoulis, "Negative index short-slab pair and continuous wires metamaterials in the far infrared regime," *Optics Express*, Vol. 16, No. 12, 9173–9180, 2008.

16. Wu, D., Y. Liu, L. Chen, R. Ma, C. Liu, C. Xiang, R. Li, and H. Ye, "Broadband mid-infrared dual-band double-negative metamaterial: Realized using a simple geometry," *Plasmonics*, Vol. 13, 1287–1295, 2018.

17. Moser, H. O., J. A. Kong, L. K. Jian, H. S. Chen, G. Liu, M. Bahou, S. M. P. Kalaiselvi, S. M. Maniam, X. X. Cheng, B. I. Wu, P. D. Gu, A. Chen, S. P. Heussler, S. bin Mahmood, and L. Wen, "Free-standing THz electromagnetic metamaterials," *Opt. Express*, Vol. 16, 13773–13780, 2008.

18. Paul, O., C. Imhof, B. Reinhard, R. Zengerle, and R. Beigang, "Negative index bulk metamaterial at terahertz frequencies," *Opt. Express*, Vol. 16, No. 9, 6736–6744, 2008.

19. Chang, C.-L., W.-C. Wang, H.-R. Lin, F. J. Hsieh, Y.-B. Pun, and C.-H. Chan, "Tunable terahertz fishnet metamaterial," *Appl. Phys. Lett.*, Vol. 102, 151903, 2013.

20. Gu, J., J. Han, X. Lu, R. Singh, Z. Tian, Q. Xing, and W. Zhang, "A close-ring pair terahertz metamaterial resonating at normal incidence," *Opt. Express*, Vol. 17, 20307, 2009.

21. Ling, F., Z. Zhong, R. Huang, and B. Zhang, "A broadband tunable terahertz negative refractive index metamaterial," *Sci. Rep.*, Vol. 8, 9843, 2018.

22. Imhof, C. and R. Zengerle, "Strong birefringence in left-handed metallic metamaterials," *Opt. Commun.*, Vol. 280, 213–216, 2007.

23. Yeh, T. T., T. Y. Huang, T. Tanaka, and T.-J. Yen, "Demonstration of a three-dimensional negative index medium operated at multiple-angle incidences by monolithic metallic hemispherical shells," *Sci. Rep.*, Vol. 7, 45549, 2017.

24. Ding, J., S. An, B. Zheng, and H. L. Zhang, "Multiwavelength metasurfaces based on single-layer dual-wavelength meta-atoms: toward complete phase and amplitude modulations at two wavelengths," *Adv. Opt. Mater.*, Vol. 5, No. 10, 1700079, 2017.

25. Kim, J. and A. Gopinath, "Simulation of a metamaterial containing cubic high dielectric resonators," *Phys. Rev. B*, Vol. 76, 115126, 2007.

26. Akmansoy, E. and S. Marcellin, "Negative index and mode coupling in all-dielectric metamaterials at terahertz frequencies," *EPJ Appl. Metamat.*, Vol. 5, 2018.

27. Koschny, Th., L. Zhang, and C. M. Soukoulis, "Isotropic three-dimensional left-handed metamaterials," *Phys. Rev. B*, Vol. 71, R121103, 2005.

28. Cheng, Y. Z., Y. Nie, and R. Z. Gong, "Broadband 3D isotropic negative-index metamaterial based on fishnet structure," *Eur. Phys. J. B*, Vol. 85, 62, 2012.

29. Engheta, N. and R. W. Ziolkowski, *Metamaterials — Physics and Engineering Explorations*, IEEE Press, 2006.

30. Beruete, M., M. Navarro-Cía, M. Sorolla, and I. Campillo, "Planoconcave lens by negative refraction of stacked subwavelength hole arrays," *Opt. Express*, Vol. 16, No. 13, 9677–9683, 2008.

31. Vodo, P., P. V. Parimi, W. T. Lu, and S. Sridhar, "Focusing by planoconcave lens using negative refraction," *Appl. Phys. Lett.*, Vol. 86, 201108, 2005.

32. Naserpour, M., C. J. Zapata-Rodríguez, C. Díaz-Aviñó, and M. Hashemi, "Metacoatings for wavelength-scale, high-numerical-aperture plano-concave focusing lenses," *J. Opt. Soc. Am. B*, Vol. 33, 2120–2128, 2016.

33. Yin, S., Y. Liang, D. Zeng, Y. Tian, P. Zhong, L. Guo, W. Huang, and W. Zhang, "Dynamic switching of coaxial focus based on terahertz meta-lens," *Appl. Opt.*, Vol. 60, 3629–3633, 2021.

34. Legaria, S., J. Teniente, S. Kuznetsov, V. Pacheco-Peña, and M. Beruete, "Highly efficient focusing of terahertz waves with an ultrathin superoscillatory metalens: Experimental demonstration," *Adv. Photonics Res.*, Vol. 2, 2000165, 2021.

35. Fu, Z., "Near-field focusing with subwavelength thickness metalenses via electromagnetic susceptibility models," *Optics and Photonics Journal*, Vol. 11, 197–209, 2021.

36. Costanzo, S., A. Borgia, I. Venneri, and G. Di Massa, "Millimeter-waves structures on benzocyclobutene dielectric substrate," *Radioengineering*, Vol. 20, 785–789, 2011.

37. Lee, D. H. and W. S. Park, "Extraction of effective permittivity and permeability of periodic metamaterial cells," *Microw. Opt. Technol. Lett.*, Vol. 51, 1824–1830, 2009.

38. Pacheco-Pena, V., B. Orazbayev, V. Torres, M. Beruete, and M. Navarro-Cıa, "Ultra-compact planoconcave zoned metallic lens based on the fishnet metamaterial," *Appl. Phys. Lett.*, Vol. 103, 183507, 2013.

39. Pendry, B., "Negative refraction makes a perfect lens," *Phys. Rev. Lett.*, Vol. 85, 3966, 2000.

40. Hashemi, M., A. Moazami, M. Naserpour, and C. J. Zapata-Rodríguez, "A broadband multifocal metalens in the terahertz frequency range," *Optics Communications*, Vol. 370, 306–310, 2016.

41. Mendis, R., M. Nagai, Y. Wang, N. Karl, and D. M. Mittleman, "Terahertz artificial dielectric lens," *Sci. Rep.*, Vol. 6, No. 1, 23023, 2016.

42. Jia, D., Y. Tian, W. Ma, X. Gong, J. Yu, G. Zhao, and X. Yu, "Transmissive terahertz metalens with full phase control based on a dielectric metasurface," *Optics Letters*, Vol. 42, No. 21, 4494–4497, 2017.

43. Zhang, H., X. Zhang, Q. Xu, C. Tian, Q. Wang, Y. Xu, Y. Li, J. Gu, Z. Tian, C. Ouyang, X. Zhang, C. Hu, J. Han, and W. Zhang, "High-efficiency dielectric metasurfaces for polarization-dependent terahertz wavefront manipulation," *Adv. Optical Mater.*, 1700773, 2017.

44. Chen, H., Z. Wu, Z. Li, Z. Luo, X. Jiang, Z. Wen, L. Zhu, X. Zhou, H. Li, Z. Shang, Z. Zhang, K. Zhang, G. Liang, S. Jiang, L. Du, and G. Chen, "Sub-wavelength tight-focusing of terahertz waves by polarization-independent high-numerical-aperture dielectric metalens," *Opt. Express*, Vol. 26, 29817–29825, 2018.

45. Jiang, X., H. Chen, Z. Li, H. Yuan, L. Cao, Z. Luo, K. Zhang, Z. Zhang, Z. Wen, L.-G. Zhu, X. Zhou, G. Liang, D. Ruan, L. Du, L. Wang, and G. Chen, "All-dielectric metalens for terahertz wave imaging," *Opt. Express*, Vol. 26, 14132–14142, 2018.

46. Cheng, Q., M. Ma, D. Yu, Z. Shen, J. Xie, J. Wang, N. Xu, H. Guo, W. Hu, S. Wang, T. Li, and S. Zhuang, "Broadband achromatic metalens in terahertz regime," *Science Bulletin*, Vol. 64, No. 20, 1525–1531, 2019.

47. Zang, X., W. W. Xu, M. Gu, B. Yao, L. Chen, Y. Peng, J. Y. Xie, A. V. Balakin, A. P. Shkurinov, Y. M. Zhu, and S. L. Zhuang, "Polarization-insensitive metalens with extended focal depth and longitudinal high-tolerance imaging," *Adv. Optical Mater.*, Vol. 8, 1901342, 2020.

48. Maruo, S. and J. Fourkas, "Recent progress in multiphoton microfabrication," *Laser & Photon. Rev.*, Vol. 2, 100–111, 2008.

49. Rill, M. S., C. Plet, M. Thiel, I. Staude, G. von Freymann, S. Linden, and M. Wegener, "Photonic metamaterials by direct laser writing and silver chemical vapour deposition," *Nature Materials*, Vol. 7, 543–546, 2008.

50. Hernandez, D. S. and J. B. Shear, "Mask-directed micro-3D printing," *Micro and Nano Technologies, Three-Dimensional Microfabrication Using Two-Photon Polymerization*, 2nd Edition, William Andrew Publishing, 2020.

51. Mao, Y., Z. Chen, J. Zhu, Y. Pan, W. Wu, and J. Xu, "Stereo metamaterial with three dimensional meta-atoms fabricated by programmable stress induced deformation for optical modulation," *2017 IEEE 30th International Conference on Micro Electro Mechanical Systems (MEMS)*, 285–288, 2017.

52. Takano, K., T. Kawabata, C.-F. Hsieh, K. Akiyama, F. Miyamaru, Y. Abe, Y. Tokuda, R.-P. Pan, C.-L. Pan, and M. Hangyo, "Fabrication of terahertz planar metamaterials using a super-fine ink-jet printer," *Appl. Phys. Express*, Vol. 3, 016701, 2010.

53. Wang, Q., B. Gao, M. Raglione, H. Wang, B. Li, F. Toor, M. A. Arnold, and H. Ding, "Design, fabrication, and modulation of THz bandpass metamaterials," *Laser & Photonics Reviews*, Vol. 13, 1900071, 2019.

54. Huang, T.-Y., C.-W. Tseng, T.-T. Yeh, T.-T. Yeh, C.-W. Luo, T. Akalin, and T.-J. Yen, "Experimental realization of ultrathin, double-sided metamaterial perfect absorber at terahertz gap through stochastic design process," *Sci. Rep.*, Vol. 5, 18605, 2015.